

## A SURVEY FOR H $\alpha$ PULSAR BOW SHOCKS

SASHA BROWNSBERGER & ROGER W. ROMANI<sup>1</sup>  
Dept. of Physics/KIPAC, Stanford University, Stanford, CA 94305-4060  
*To appear in ApJ*

### ABSTRACT

We report on a survey for H $\alpha$  bow shock emission around nearby  $\gamma$ -detected energetic pulsars. This survey adds three Balmer-dominated neutron star bow shocks to the six previously confirmed examples. In addition to the shock around *Fermi* pulsar PSR J1741–2054, we now report H $\alpha$  structures around two additional  $\gamma$ -ray pulsars, PSR J2030+4415 and PSR J1509–5850. These are the first known examples of H $\alpha$  nebulae with pre-ionization halos. With new measurements, we show that a simple analytic model can account for the angular size and flux of the bow shocks' apices. The latter, in particular, provides a new pulsar probe and indicates large moments of inertia and smaller distances than previously assumed, in several cases. In particular we show that the re-measured PSR J0437–4715 shock flux implies  $I = (1.7 \pm 0.2) \times 10^{45} / (f_{HI} \sin i) \text{g cm}^2$ . We also derive a distance  $d \approx 0.72 \text{ kpc}$  for the  $\gamma$ -ray only pulsar PSR J2030+4415 and revised distances for PSRs J1959+2048 (1.4 kpc) and J2555+6535 ( $\sim 1 \text{ kpc}$ ), smaller than the conventional DM-estimated values. Finally we report upper limits for 94 additional LAT pulsars. An estimate of the survey sensitivity indicates that for a warm neutral medium filling factor  $\phi_{WNM} \sim 0.3$  there should be a total of  $\sim$  nine H $\alpha$  bow shocks in our LAT-targeted survey; given that seven such objects are now known, a much larger  $\phi_{WNM}$  seems problematic. *Subject headings:* Gamma rays: stars - pulsars: individual PSR J2040+4415 - pulsars: individual PSR J1509–5850 - Shock waves

### 1. INTRODUCTION

Pulsar wind nebulae (PWNe) have been observed *via* X-ray synchrotron radiation for many sources over many years (Kargaltsev & Pavlov 2010, and references therein). These data probe the bulk energetics of the pulsar wind and, with high quality images from the *Chandra* X-ray observatory, reveal termination shock structure in the form of tori and jets. When the pulsar is subsonic, as in their parent supernova remnant, these X-ray structures can show high symmetry about the spin axis. However, when the pulsar escapes to the cooler external interstellar medium (ISM), the pulsar motion is generally supersonic and the termination shocks are ram pressure confined due to the pulsar motion. This asymmetry can distort the relativistic PWN termination shock. Thus it was particularly interesting when an H $\alpha$  bow shock was discovered around the black widow millisecond pulsar PSR B1957+20 (Kulkarni & Hester 1988), both because this structure showed high symmetry about the pulsar velocity axis and because the Balmer line emission allows kinetic study of the shock structure. These bow shocks are non-radiative, with the pulsar velocity ensuring that the shocked ISM flows well down-stream before it cools. Non-radiative shocks show extreme Balmer domination and the velocity structure of these lines turns out to be a sensitive probe of the shock physics, including information on the up-stream ISM, the post-shock flow and even supra-thermal particle acceleration (Wagner et al. 2009). Pulsar bow shocks have an interesting range of speeds (low com-

pared to most supernova remnants) and shock obliquities, so observation of these nebulae provide an excellent opportunity to study non-radiative shock physics.

Given this interest, a number of searches have been mounted for similar pulsar nebulae (e.g. Cordes et al. 1993; Gaensler et al. 2002), with some limited success. Before the present search there were six confirmed H $\alpha$  pulsar bow shocks reported in the literature. A shock around PSR J1741–2054 was discovered in the initial phase of the present search (Romani et al 2010). A few other candidates have been presented in the literature, but clearly these objects are quite rare.

We report here on a new sensitive survey of a large number of nearby energetic pulsars. We have tested this sensitivity with images of known bow shocks. Despite the modest exposures, these are in general comparable with or superior to earlier images in the literature, and show additional interesting H $\alpha$  structure. Our survey has added three new bow shock detections (two reported here for the first time). We use the new measurements, and a re-assessment of the other known bow shocks, to illustrate the dependence on pulsar properties. In addition we derive quantitative upper limits on the H $\alpha$  fluxes from the non-detections. This is now a large enough sample that it can be used to evaluate, heuristically, the detection probability's dependence on pulsar parameters. Also, for a basic assumed model, the limits provide an interesting spot sample of the neutral ISM within a few kpc of the Sun.

### 2. BOW SHOCK BASICS

One can estimate the spin-down luminosity of a rotation-powered pulsar as  $\dot{E} = 4\pi^3 I \dot{P} / P^3$ . Conventionally one assumes  $I = 10^{45} \text{g cm}^2$ . However, van Kerkwijk & Kulkarni (2011) have estimated the mass of PSR J1959+2048 as  $2.4 \pm 0.16 M_{\odot}$ . To accommodate such a large mass, the equation of state must be stiff, and the moment of inertia correspondingly large. Lattimer & Schutz (2005) find that for stiff equations

rwr@astro.stanford.edu, sashab@stanford.edu

<sup>1</sup> Visiting Astronomer, Kitt Peak National and Cerro Tololo Inter-American Observatories, which are operated by the Association of Universities for Research in Astronomy (AURA) under cooperative agreement with the National Science Foundation. The WIYN observatory is a joint facility of the University of Wisconsin-Madison, Indiana University, Yale University, and the National Optical Astronomy Observatory. The SOAR telescope is a joint project of: Conselho Nacional de Pesquisas Cientificas e Tecnologicas CNPq-Brazil, The University of North Carolina at Chapel Hill, Michigan State University, and the National Optical Astronomy Observatory.

of state the moment of inertia is approximately

$$I \approx (0.8 - 1.2) \times 10^{45} M^{1.5} \text{g cm}^2 \quad (1)$$

where the mass is measured in solar masses and the prefactor covers the range allowed by the equations of state that can accommodate PSR J1959+2048's mass (from AP4 to the most extreme MS0, in their compilation). To be conservative, we adopt here the smaller coefficient in this estimate and for sources without published neutron star mass measurements we will assume  $1.4M_\odot$  ( $I_{45} = 1.3$ ) for young pulsars and  $1.8M_\odot$  ( $I_{45} = 1.9$ ) for strongly recycled millisecond pulsars. Our analysis is not very sensitive to this parameter. A more detailed sum could include a mass distribution (e.g. Özel et al. 2012), but this should be computed for the short period, very energetic LAT sample, including black-widow type pulsars.

For radio pulsars we have a distance estimate  $d$  from the dispersion delay or, less often, but much more reliably, a parallax measurement from pulse timing or interferometry. These are often supplemented by proper motion estimates  $\mu$ , so that we can infer a transverse space velocity  $v = 4.75\mu_{\text{masy}}d_{\text{kpc}}/\sin i \text{ km s}^{-1}$ , where  $\mu_{\text{masy}}$  is measured in milli-arcseconds/year,  $d_{\text{kpc}}$  is the distance in kiloparsecs and  $i$  the angle between  $\vec{v}$  and the Earth line-of-sight. This velocity can be used to correct the observed spindown for the Shklovskii (1970) effect

$$\dot{P} = \dot{P}_{\text{obs}} - 2.43 \times 10^{-21} P \mu_{\text{masy}}^2 d_{\text{kpc}} \quad (2)$$

which can be substantial for high velocity millisecond pulsars. We ignore here the smaller perturbations to  $\dot{P}_{\text{obs}}$  caused by acceleration in the Galactic potential. Equations (1) and (2) improve our estimate of the pulsar spin-down luminosity  $\dot{E}$ .

An  $\text{H}\alpha$  bow shock forms when a pulsar of luminosity  $10^{34} \dot{E}_{34} \text{erg s}^{-1}$  travels supersonically through a partly neutral medium of density  $\rho = \gamma_H m_p n_H$ . Along  $\vec{v}$  the pulsar wind and ISM ram pressure balance at the contact discontinuity at standoff angle

$$\theta_0 = (\dot{E}/4\pi c \rho v^2)^{1/2}/d. \quad (3)$$

The  $\text{H}\alpha$ -producing forward shock lies upstream, at an apex distance of  $\theta_a \approx (1.3 - 1.5) \times \theta_0$  (Aldcroft et al. 2002; Bucciantini 2002), so we infer a characteristic angular scale for the bow shock apex of

$$\theta_a = 1.3\theta_0 = 19.7'' [\dot{E}_{34} \sin^2 i / (n_H \mu_{\text{masy}}^2)]^{1/2} d_{\text{kpc}}^{-2}, \quad (4)$$

using  $\gamma_H = 1.37$  to convert H density to total density. In the simple case of a spherically symmetric wind Wilkin (1996) has provided a convenient analytic description of the contact discontinuity stand-off for the thin-shock case

$$r(\phi) = r_0 [3(1 - \phi \cot \phi)]^{1/2} / \sin \phi \quad (5)$$

where  $\phi$  is measured from the direction of motion with respect to the ambient ISM. As noted by Romani et al (2010), for such a wind the projected angle to the bow shock limb at the apex is nearly independent of  $i$ , as long as  $i$  is not very small. Numerical simulation (eg. Bucciantini 2002) shows that finite pressure causes the forward shock to thicken slightly along the bow shock; in the vicinity of the pulsar this is well approximated by increasing the transverse size to

$$r_\perp = 1.25 \times 1.3 r(\phi) \sin(\phi) \quad (6)$$

over a few  $\times \theta_a$ .

Further downstream, bow shocks are visible to  $100 \times \theta_a$  and a wide range of structures are seen, often with multiple cavities or bubbles, suggesting either ISM density variations or  $\dot{E}$  instabilities (van Kerkwijk & Ingle 2008). Also, Wilkin (2000) extended the thin shock analysis to give expressions for the more general case of an axisymmetric wind, possibly misaligned with the pulsar motion. Indeed a few bow shock limb shapes are best fit including an equatorial concentration for the pulsar wind (Vigelius et al. 2007; Romani et al 2010).

However, near the apex all observed bow shocks have a similar shape, allowing reasonable estimates for the standoff scale and flux by measuring in an aperture following equations (5) and (6). We define the apex zone from  $\theta_a$  ahead of the pulsar to  $-2\theta_a$  behind. Study of this zone, when resolved, allows useful comparison between bow shocks (although as noted for a few cases detailed fits to the limb give significant constraints on velocity inclination  $i$  and wind asymmetry). From Equation (5) the apex region extends  $2.77r_a$  transverse to the direction of motion, and so, including our approximation for the forward shock thickness, the apex sweeps up a flux of

$$\dot{N} = \pi(3.45r_a)^2 v n_H f_{HI} \quad (7)$$

neutral H atoms per second, where  $f_{HI}$  is the neutral fraction. These neutrals pass into the heated, shocked ISM where they suffer collisional excitation and charge exchange before ionization at a distance  $l \approx v/(R_I n) \sim (1-3) \times 10^{15} v_7 n^{-1} \text{cm}$ , with the ionization rate  $R_I \sim (0.3-1) \times 10^{-8} \text{cm}^3 \text{s}^{-1}$  in the bow shock velocity regime  $v = 10^7 v_7 \text{cm s}^{-1}$ . Note that

$$l/r_a \approx 10^{-4} (\mu_{\text{masy}} d_{\text{kpc}} / \sin i)^2 (n_H \dot{E}_{34})^{-1/2} \quad (8)$$

so  $l \ll r_a$  except for the highest velocity low luminosity pulsars; we expect that the  $\text{H}\alpha$ -emitting layer is thin and that the ISM is generally fully ionized before the contact discontinuity. For non-radiative shocks in supernova, the rule of thumb is  $\epsilon_{\text{H}\alpha} \sim 0.2$  emitted  $\text{H}\alpha$  photons per incoming neutral (Raymond 2001). However our pulsar bow shocks have relatively low velocities  $v_7 = 1-10$ , and the computations of Heng & McCray (2007) indicate increased  $\text{H}\alpha$  yield for  $v < 10^3 \text{km s}^{-1}$

$$\epsilon_{\text{H}\alpha} \approx 0.6 v_7^{-1/2} \quad (9)$$

if the post-shock electrons and ions equilibrate via plasma-wave interactions. If out of equilibrium, the yield appears to be lower at small velocity with  $\epsilon_{\text{H}\alpha} \approx 0.04 v_7^{3/4}$ . Together these estimates give an  $\text{H}\alpha$  flux at Earth of

$$\begin{aligned} f_{\text{H}\alpha} &= \dot{N} \epsilon_{\text{H}\alpha} / (4\pi d^2) \\ &= 3.5 \times 10^{-2} \dot{E}_{34} \sin^3 i f_{HI} \mu_{\text{masy}}^{-3/2} d_{\text{kpc}}^{-7/2} \text{cm}^{-2} \text{s}^{-1} \end{aligned} \quad (10)$$

where we assume post-shock  $e^-$ -ion equilibration and have not explicitly included the dependence of  $\dot{E}_{34}$  on velocity or neutron star mass. One should note that the apex  $\text{H}\alpha$  flux is essentially independent of the density  $n$  as long as the ISM is fully ionized before the momentum balance at the contact discontinuity.

The LAT-selected pulsars are energetic and in nearly all cases have very small  $l/r_a$  (equation 8). However, the two non-LAT pulsars J1856-3754 and J2225+6535 are high velocity, low  $\dot{E}$  objects and we expect incomplete ionization at the bow shock apex. This is case A of Bucciantini & Bandiera (2001). Here we expect the momentum balance to be determined by the post shock ionized fraction. This will be a com-

bination of the upstream ionization fraction  $x_i = (1 - f_{\text{HI}})$  and incomplete post-shock ionization prior to the contact discontinuity with fraction  $\approx 0.3 r_a/l$ . If

$$x_i > 340(\dot{E}_{34}n)^{1/3}[\sin i/(\mu_{\text{masy}}d_{\text{kpc}})]^{4/3} \quad (11)$$

then the former dominates (case A1) and the standoff angle (4) increases by  $x_i^{-1/2}$  (or the density inferred from a measured  $\theta_a$  increases by  $1/x_i$ ). The minimum pre-ionization fraction satisfying equation (11) is

$$x_i = 351(\dot{E}_{34}/\theta_a)^{1/2}(\sin i/\mu_{\text{masy}})^{3/2}d_{\text{kpc}}^{-2} \quad (12)$$

where the observed standoff angle  $\theta_a$  is in arcseconds, and sensible values obtain for the strong case A (small  $\dot{E}_{34}$ , large  $\mu_{\text{masy}}$ ) limit. In turn this gives the maximum apex flux for case A1, which is increased from equation (10) by  $(1-x_i)/x_i$ .

In contrast, if the preshock ionization fraction is sufficiently low, then post-shock ionization can dominate and from equation (4), replacing  $n_H$  with  $0.3 r_a n_H/l$ , we find (case A2)

$$\theta_a = 1.6''[\dot{E}_{34}\sin i/(n^2\mu_{\text{masy}}d_{\text{kpc}}^4)]^{1/3} \quad (13)$$

and

$$f_{\text{H}\alpha} = 2.4 \times 10^{-4} f_{\text{HI}} \left( \frac{\dot{E}_{34}\sin i}{n_H^2\mu_{\text{masy}}d_{\text{kpc}}^3} \right)^{1/6} \text{ cm}^{-2} \text{ s}^{-1} \quad (14)$$

where the prefactors are doubtless somewhat sensitive to the details of the postshock ionization, which can in principle be measured from flux profile at the limb of well-resolved bow shocks. Notice that in case A2  $f_{\text{H}\alpha}$  does depend on the total upstream H density  $n_H$ .

### 2.1. Survey Target Selection

From these expressions we see that a bow shock should have large  $\theta_a \propto \dot{E}^{1/2}/d^2$  to be resolvable and large  $f_{\text{H}\alpha} \propto \dot{E}/d^{7/2}$  to be bright. Thus, nearby, powerful pulsars should dominate the bow shock sample. The most extensive uniform compilation of such pulsars comes from the *Fermi* LAT, where in the second pulsar catalog (Abdo et al. 2013, hereafter 2PC) 117  $\gamma$ -ray pulsars are presented. This represents an approximately flux limited sky survey. In this catalog, it was noted that the pulsar  $\gamma$ -ray luminosity scales, heuristically, as

$$L_\gamma \approx (10^{33} \text{ erg s}^{-1} \dot{E})^{1/2}, \quad \dot{E} > 10^{33} \text{ erg s}^{-1}, \quad (15)$$

so the flux at Earth scales as  $f_\gamma \propto \dot{E}^{1/2}/d^2$ . Interestingly, this means that (for  $\mu$ ,  $f_{\text{HI}}$  etc. fixed) that we have an approximate scaling  $f_{\text{H}\alpha} \sim f_\gamma^2$ . Thus bright  $\gamma$ -ray pulsars have the potential to show bright, resolvable H $\alpha$  bow shocks.

In view of the above, it is not surprising that most of the bow-shock producing pulsars, both young and millisecond pulsars (MSP) are LAT-detected. The exceptions are PSR J2225+6535 and J1856–3754, both low  $\dot{E}$ , high  $v$  (case A) objects. PSR J1856–3754 is also very nearby and, lacking any non-thermal pulse detection, may be beamed away from Earth. Thus, in searching for new pulsar H $\alpha$  bow shocks we focused on the LAT pulsars from 2PC and on nearby, energetic pulsars newly discovered in the direction of *Fermi* LAT sources (eg. Ray et al. 2012; Pletsch et al. 2013).

## 3. OBSERVATIONS

Our pulsar H $\alpha$  campaign was pursued during a series of WIYN and SOAR observations, allocated through the joint

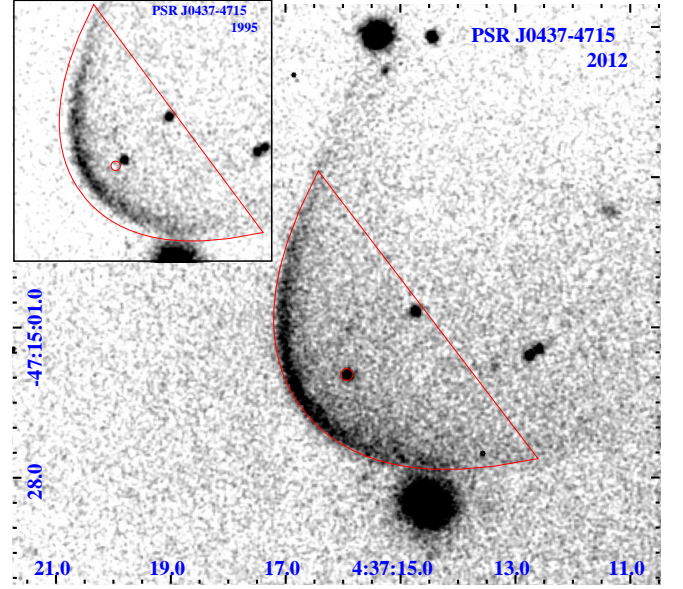


FIG. 1.—  $3 \times 600$  s W012 SOI image of PSR J0437–4715. The line delimits the apex region (eqs. 4–6). The inset shows a 1995 H $\alpha$  image (Andy Fruchter, <http://www.stsci.edu/~fruchter/nebula>), with the 2012 apex region and pulsar location indicated, for comparison. The visible pulsar companion and shock limb shift by  $2.4''$ , as expected.

*Fermi*/NOAO program to study the counterparts of LAT pulsar, blazar and unidentified sources. The PWN data reported here came from portions of five observing runs, covering both the Northern and Southern hemispheres. For all H $\alpha$  images we used the WIYN W012 ( $\lambda = 6566\text{\AA}$ ,  $\Delta\lambda_{\text{FWHM}} = 16\text{\AA}$ ) narrow band H $\alpha$  filter, kindly loaned to SOAR for the two southern campaigns. To help distinguish poorly-resolved H $\alpha$  sources near the pulsars from stars, we also obtained, when possible, matching continuum observations using the W014 ( $\lambda = 6562\text{\AA}$ ,  $\Delta\lambda_{\text{FWHM}} = 378\text{\AA}$ ) wide H $\alpha$  filter or an SDSS  $r'$  ( $\lambda = 6163\text{\AA}$ ,  $\Delta\lambda_{\text{FWHM}} = 1518\text{\AA}$ ) broad band filter.

### 3.1. WIYN Campaigns

In the North, we used the WIYN 3.6m telescope and the MiniMo camera, with observations occurring on 2009 March 24–26, 2011 September 26–27 and 2012 February 17–18. The MiMo camera is a two chip mosaic, with  $0.14''$  pixels covering a  $10'$  Field of View (FOV), with a  $7''$  gap. The pulsar H $\alpha$  survey was the ‘poor seeing’ portion of the program and so generally images were taken under  $0.9$ – $1.4''$  imaging. Despite the imaging limitations, we were able to maintain relative photometry to  $\sim 10\%$ , and substantial portions of the 2011 and 2012 runs were near-photometric.

In total 52 unique LAT pulsars were observed at WIYN (9 in 2009, 33 in 2011, 21 in 2012, some re-observed). Typical initial exposures were 300s or 600s, objects showing promising structure near the pulsar position received a second exposure. Unfortunately, the relatively long MiMo read-out time (182s for a full frame) made short exposures inefficient and so continuum frames (30–60s) were only obtained for a few pulsars. We observed the compact Balmer-dominated planetary nebula M1-5=PN G184.0-0.21 (Wright et al. 2005) to establish our flux scale at  $4.8 \times 10^{-5} \text{ H}\alpha \text{ cm}^{-2} \text{ s}^{-1} / \text{DN}$ .

### 3.2. SOAR Campaigns

We observed with the SOAR Optical Imager (SOI) on the 4.2m SOAR telescope on March 21–23, 2012. SOI has  $0.078''$

native pixels in a 2 CCD mosaic covering a  $5.3'$  FOV with a  $7.8''$  gap. As we did not experience exceptionally good seeing, we ran binned  $2 \times 2$ , for a  $0.15''$  pixel scale and an excellent read-out time of 11 s. Again the best seeing during the run was allocated to a different component of the program (BL Lac imaging) and pulsar  $H\alpha$  images had typical  $0.8$ - $1.2''$  delivered image quality. The loss of mirror temperature control during the second half of the run adversely affected image quality. We observed 29 pulsar targets during this run.  $H\alpha$  flux calibrations were generated from exposures of PN G232.8-04.7 (Dopita & Hua 1997), giving  $5.9 \times 10^{-5} H\alpha \text{ cm}^{-2} \text{ s}^{-1} / \text{DN}$ . 60 s W014 frames were obtained for most targets to discriminate against continuum structures.

We returned to SOAR on August 9-12, 2013, but for this run, the need for interleaved spectroscopy plus limited resources for instrument changes led us to use the Goodman High-Throughput Spectrograph (GHTS) for the imaging. Although GHTS has  $0.15''$  pixels covering a  $7.2'$  diameter FOV, the long 96s read-down led us to sub-frame to a  $4.25' \times 6.5'$  field. In addition, poor seeing caused us to bin  $2 \times 2$  after the first night, resulting in a modest 15 s readout. The seeing was highly variable during the run, with brief periods at  $\sim 1''$ , but typical seeing of  $2''$ , and periods over  $5''$ . The last night was largely lost to weather. Unfortunately, GHTS suffered electronic pick-up during this run, leading to a variable baseline modulation of  $\sim 10\text{DN}$  beyond the nominal read-out. Because of the very narrow W012 band-pass, sky count-rates were low and this modulation dominated the background, limiting our sensitivity to low surface brightness structures. Exposures were thus 600 s in the W012 filter. Calibration observations of the planetary nebula BoBn 1 (Wright et al. 2005) gave throughput estimates. However cross-comparison with fields common to the SOI and MiMo runs indicated that the flux scale from this calibrator was high by 20%. Our adopted flux conversion after this correction was  $5.1 \times 10^{-5} H\alpha \text{ cm}^{-2} \text{ s}^{-1} / \text{DN}$ , and we estimate the uncertainty in the relative (and absolute) calibrations for the three systems as  $\sim 10\%$ , both due to imperfect instrumental calibration and imperfect monitoring of transparency. For this run, we elected to obtain SDSS  $r'$  continuum frames (typically 180 s exposure), which gave us adequate sensitivity to contaminating stars. This also allowed modest sensitivity to stellar companions of binary LAT MSP, despite the very poor imaging conditions.  $H\alpha$  limits were obtained for 20 LAT pulsars in this run.

#### 4. MEASUREMENT AND RESULTS

The data were subject to standard IRAF calibrations, with image bias subtraction and correction using dome and sky flats. World coordinate systems were applied to the the frames, as appropriate, and the images were combined with a median filter, clipping cosmic ray events.

##### 4.1. New Images of Known Bow Shocks

To ensure that our survey sensitivity was sufficient to routinely detect pulsar bow shocks, we imaged several known objects. We observed J0437-4715 (March 22, 2012, with SOI), where it was obvious in a single 300 s exposure. In Figure 1 we show a combination of 1800 s exposure under  $\sim 1.2''$  imaging. The region shows our ‘apex’ zone from equations (5) and (6); these provide a very good match to the apex shape with an effective standoff angle  $\theta_a = 9.3''$ . In the inset we show this 2012 epoch shock limb and pulsar position on a

1995 image, showing the motion of the companion and bow shock apex over 17 years.

Bell et al. (1995) give the  $H\alpha$  flux of this nebula as  $2.5 \times 10^{-3} \text{ cm}^{-2} \text{ s}^{-1}$ , and this has been widely quoted. We have measured the  $H\alpha$  flux in the apex zone (expanded slightly to account for the image FWHM) and find  $6.7 \pm 0.7 \times 10^{-3} \text{ cm}^{-2} \text{ s}^{-1}$ . We also took  $2 \times 600$  s exposure with the GHTS on August 17, 2013. Although the seeing was very poor we were able to confirm the large flux, obtaining  $\approx 6.9 \pm 1.0 \times 10^{-3} \text{ cm}^{-2} \text{ s}^{-1}$ , where the uncertainty is dominated by the choice of background for this large diffuse nebula. The full nebula contains  $\sim 60\%$  more flux. Thus we find the the  $H\alpha$  bow shock flux of PSR J0437-4715 is  $2.7 - 4.3 \times$  larger (depending on region) than previously reported; this will be important to our discussion below.

To check sensitivity against the faintest young radio pulsar bow shock reported in the literature, we also observed PSR J0742-2822 with SOI. Here the shock was clear in a single 600 s exposure. Figure 2 shows a  $3 \times 600$  s median stack. Guided by the 6500 s NTT discovery image of Jones et al. (2002), we centered the pulsar on one of the array chips; we see a rather similar ‘keyhole’ shape at the apex. However, our combined data show that the nebula extends much further than previously reported. Jones et al. (2002) suggest that the nebula closes off some  $45''$  behind the pulsar but we see the wedge of  $H\alpha$  emission extending off of our frame, over  $2.5 \times$  further. This tail shows multiple swellings reminiscent of the bubbles of PSR J2225+6535/Guitar nebula. Doubtless faint emission extends beyond our image, so we have not captured the full size of this nebula. These data confirm that the very narrow bandpass of the W012 filter provides excellent contrast for the  $H\alpha$  emission; although the image is count limited, we obtain S/N comparable to that of Jones et al. (2002) in  $\sim 1/5$  the exposure time.

Similarly we observed the faintest known MSP bow shock, that discovered by Gaensler et al. (2002) around PSR J2124-3358 in a 4800 s NTT image stack. We exposed a single 600 s frame, using the GHTS on August 10, 2013, under poor ( $\sim 2''$ ) seeing and with the large pattern noise at read-out. Nevertheless, this image (Figure 3) shows more structure than the discovery data – for example the nebula narrows to the north of the pulsar, making the bulk of the body into a cavity. Also there is no sign of the filament to the East of the PWN seen in the NTT data; this may have been an optical artifact during that exposure. However the ‘kink’ structure on the east of the bow shock and the bright limb at the apex are very well measured. Again, this good detection gives us confidence that we would usually detect structures as bright as those previously reported in the literature.

##### 4.2. New Pulsar $H\alpha$ Structures

We briefly describe the morphology and flux of the newly detected  $H\alpha$  structures to facilitate comparison with previously known bow shocks and our survey upper limits. Detailed modeling and multiwavelength analysis is deferred to future publications. We discuss the novel pre-ionization structures seen for PSR J1509-5850 and J2030+4415 in §4.4

The bow shock of PSR J1741-2054 has been described in Romani et al (2010). It is quite bright, but lies in a very crowded Galactic field. This nebula hosts a bright X-ray PWN, which trails off to the NE along the  $H\alpha$  minor axis. Perhaps the most interesting aspect of this PWN is that the pulsar lies rather close to the forward shock apex in projection and the apex curvature is small; it was argued that this indi-

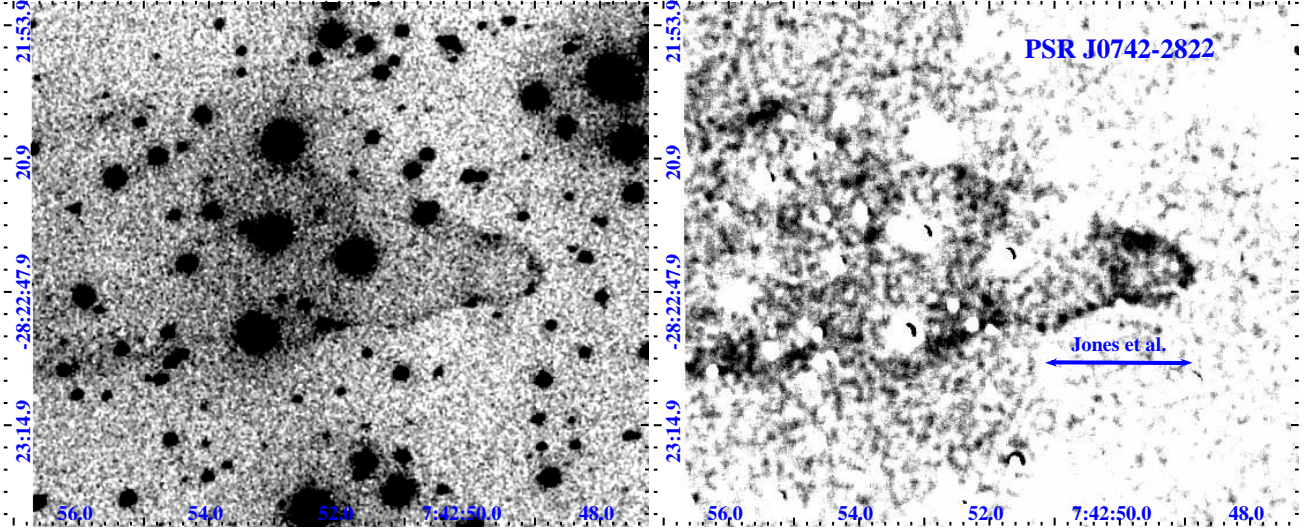


FIG. 2.— Left: a median-filtered  $3 \times 600$  W012 SOI image of PSR J0742–2822, smoothed with a  $0.45''$  Gaussian. The right panel shows an image with a scaled continuum (W014) image subtracted and  $0.9''$  top-hat smoothing. The arrow indicates extent of the previous nebula detection.

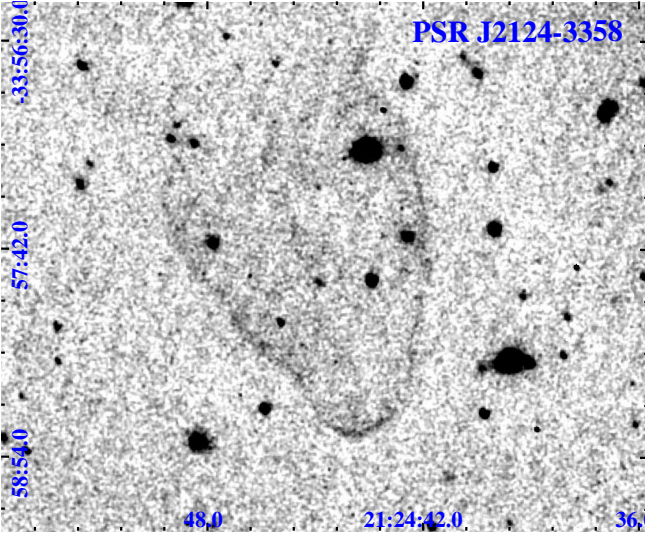


FIG. 3.— 600 s W012 GHTS image of PSR J2124–3358, smoothed with a  $0.9''$  Gaussian. The bow shock narrows  $70''$  behind the pulsar but appears to continue faintly to larger  $r/r_a$ . The background diagonal striations are pick-up noise during read-out.

icates an equatorially concentrated pulsar wind. As for PSR J2124–3358, this induces us to use a  $\theta_a \approx 2 \times$  larger than the observed standoff to set the apex scale and the effective apex H $\alpha$  flux in Table 1.

PSR J2030+4415 is a 227 ms,  $\dot{E}_{34} = 2.2$  pulsar found in a blind search of an unidentified *Fermi* source (Pletsch et al. 2012). This pulsar has not been detected in the radio. Figure 4 shows a  $3 \times 600$  s W012 frame taken September 26, 2011 with WIYN/MiMo, showing a very bright compact H $\alpha$  bow shock coincident with the pulsar. The apex stand-off is estimated as  $\theta_a = 1''$ , while the apex zone provides  $2.4 \times 10^{-3} \text{cm}^{-2} \text{s}^{-1}$ . After the apex, the PWN shows a closed bubble covering  $\sim 15 \times 25''$ . The apex appears partly superimposed on this bubble, so the pulsar velocity may have significant inclination to the plane of the sky. The region shows extensive diffuse H $\alpha$  emission, yet the sharpness of the nebula limb indicates that the pulsar is embedded in largely neutral H.

This pulsar lacks any parallax or DM distance estimates. However, we can get a crude estimate for the distance by in-

voking the phenomenological  $\gamma$ -ray luminosity law (equation 15) to find

$$d_\gamma = (f_\Omega L_\gamma / 4\pi F_\gamma)^{1/2} \approx 1.6 \text{kpc} (f_\Omega / F_{-11})^{1/2} \dot{E}_{34}^{1/4} \quad (16)$$

where the LAT flux is  $F_{-11} 10^{-11} \text{erg cm}^{-2} \text{s}^{-1}$  and the  $\gamma$ -ray beaming fraction is typically  $f_\Omega \approx 1$ , although it can range from  $\approx 0.1 - 3$  depending on the pulsar magnetic inclination  $\alpha$  and viewing angle  $\zeta$  (Watters et al. 2009). With an observed  $\gamma$ -ray flux  $F_{-11} = 5.8$  for PSR J2030+4415 (2PC) we infer a distance  $d = 0.88$  kpc.

One interesting feature of this bow shock is the faint diffuse H $\alpha$  seen ahead of the apex shock limb. This is likely photoionization; we have examined 14 ks of archival SWIFT XRT data and see a clear detection of the pulsar/PWN, with an unabsorbed 0.3–10 keV flux of  $1.4 \times 10^{-13} \text{erg cm}^{-2} \text{s}^{-1}$ , for a typical  $\Gamma = 2$  and  $N_H \approx 3 \times 10^{21} \text{cm}^{-2}$ . While these values require confirmation from higher sensitivity X-ray observation, this implies an X-ray luminosity  $L_X \sim 1.6 \times 10^{31} d_{\text{kpc}}^2 \text{erg s}^{-1}$  from the vicinity of the pulsar.

In Figure 5 we show H $\alpha$  structure associated with the young ( $P = 89$  ms,  $\tau = 1.5 \times 10^5 \text{y}$ ) energetic  $5.2 \times 10^{35} \text{erg s}^{-1}$  radio/ $\gamma$  pulsar J1509–5850. This pulsar has a long  $> 8'$  PWN trail observed in the radio (Ng et al. 2010) and X-ray (Kargaltsev et al. 2008). The X-ray flux of the PWN is  $\sim 2.4 \times 10^{-13} \text{erg cm}^{-2} \text{s}^{-1}$ , with  $\sim 1/2$  of this flux from near the pulsar position. In the right panel we overlay a portion of this X-ray trail from a 40 ks archival *CXO* image (OBSID 3513). The brightest arc of the extended emission follows the bow shock structure near the pulsar. With a DM estimated distance of 2.6 kpc, this apex region is relatively luminous with  $L_X > 1 \times 10^{32} \text{erg s}^{-1}$ . When smoothed on larger scales fainter X-ray emission is visible, extending some  $8'$  behind the pulsar. An additional 380 ks of *CXO* exposure is being collected on this pulsar, which should allow an excellent study of the arcsec-scale X-ray PWN and its relation to the H $\alpha$  structure.

In contrast to J2030+4415, the H $\alpha$  emission is dominated by a spherical halo centered on the pulsar, almost certainly due to X-ray excitation of the upstream medium. The most prominent feature of the bow shock is the cavity in this halo, where the relativistic pulsar wind eliminates the HI. How-

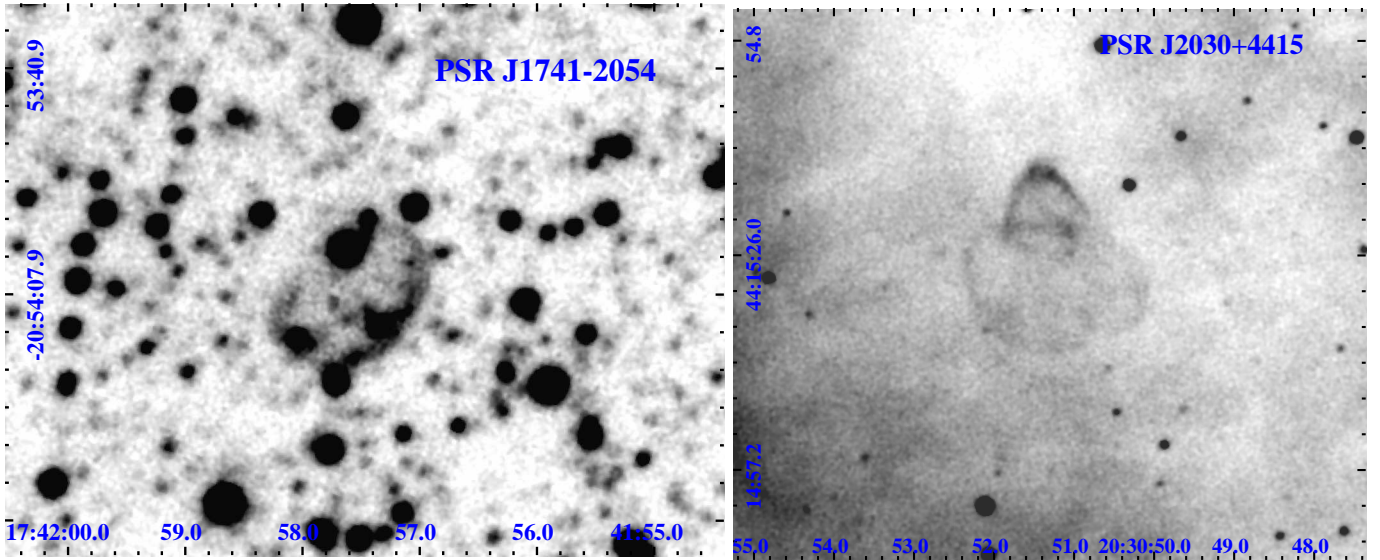


FIG. 4.— Left: a median-filtered 1800 s W012 MiMo image of PSR J1741–2054, smoothed with a  $0.45''$  Gaussian (Romani et al 2010). Right: median-filtered  $3 \times 600$  W012 MiMo image of LAT pulsar PSR J2030+4415, embedded in diffuse  $H\alpha$ . Faint emission appears  $\sim 2''$  ahead of the bow shock.

ever, this cavity is significantly edge-brightened, indicating that the upstream medium shocks and that the  $H\alpha$  surface brightness increases in this zone. The brightest limb patches (where the bow shock flares well behind the pulsar) have a surface brightness peaking at  $\sim 4 \times 10^{-5} \text{cm}^{-2} \text{s}^{-1} \text{arcsec}^{-2}$ , although the average brightness along the limb is  $\sim 10 \times$  less. We estimate a standoff scale  $\theta_a = 1.2''$  and a flux  $1.4 \times 10^{-4} \text{cm}^{-2} \text{s}^{-1}$ . This is embedded in a halo of radius  $30''$  and flux  $6.6 \times 10^{-3} \text{cm}^{-2} \text{s}^{-1}$ . These structures have high statistical significance, but given the rather low  $H\alpha$  surface brightness they are not visually striking; we outline their edges in the right panel to guide the eye.

#### 4.3. The $H\alpha$ Pulsar Bow Shocks

Scaling laws for the flux of  $H\alpha$  bow shock emission have in the past attempted to model the entire shock flux. This is difficult as the detailed limb shape and emissivity seem to be strongly dependent on local variation in the ISM and possibly on instabilities in the back-flow of the shocked relativistic pulsar wind (e.g. J0742–2822, J2030+4415 and J2225+6563). Some studies (e.g. Cordes et al. 1993; Chatterjee & Cordes 2002) suggest that with higher pulsar velocity the shock can support  $H\alpha$  production with an increasingly oblique shock so that the total  $H\alpha$  flux scaled as  $\sim v^3$ . This is physically plausible, but certainly subject to the ISM variation and instabilities noted above. In contrast, when the pulsar apex region is resolved, the bow shock geometries are very similar. We choose here to concentrate on this region as it has the best hope of correlating with, and being a useful probe of, the pulsar properties.

To this end, we compile in Table 1 the observed properties for the pulsars with resolved  $H\alpha$  emission at the apex. The spindown powers listed have been corrected for the Shklovskii (1970) effect at the default distance.

For six of these pulsars we measured the bow shock apex scales and fluxes from our calibrated images (Figures 1-5), and estimated the full extent of the  $H\alpha$  emission. It is difficult to assign flux errors, as these are dominated by uncertainty in the definition of the nebula boundary, exclusion of faint continuum sources and, for the larger nebulae, removal of the

spatially variable diffuse background. We estimate  $\sim 20\%$  for these systematic errors. For J1741–2054 and J2124–3358, the flattened apex indicates an equatorially concentrated pulsar wind (Romani et al 2010) – for these we use an apex zone scaled to an effective standoff  $\theta_a \approx 2 \times$  the actual distance from the pulsar to the shock limb; this better fits the curvature of the apex and estimates the ISM cross section.

We do not have new images for three of the bow shocks. For J1856–3754 we scale from the  $2 \times 10^{-5} \text{H}\alpha \text{cm}^{-2} \text{s}^{-1}$  (within a perpendicular distance of  $2''$ ) given by van Kerkwijk & Kulkarni (2001), the estimate of the full bow shock flux as  $\sim 3 \times$  that of the apex is rough as it becomes faint downstream. For J1959+2048, in archival images we find for the full nebula a somewhat smaller flux than the  $7.3 \times 10^{-3} \text{cm}^{-2} \text{s}^{-1}$  given by Kulkarni & Hester (1988). The tabulated apex flux comes from a new calibrated integral field observation of the nebula (integrating over the  $H\alpha$  line); we cross check this flux against observations of J1741–2054 from the same night. These data will be described elsewhere (Romani et al. 2014, in prep.). For J2225+6535 we have used the calibrated archival *Hubble Space Telescope* WFPC2 images described by Chatterjee & Cordes (2002). Like these authors, we find that the apex varies significantly between the two epochs, with  $\theta_a \approx 0.10''$  in 1994 and  $\approx 0.14''$  in 2001; the surface brightness is  $\sim$ constant and the apex flux is  $\sim 3 \times$  brighter in 2001. Table 1 lists the average of these epochs. The ‘total’ length and flux are for the guitar head as this seems to correspond most closely to the other bow shocks. Including the guitar body, the full nebula extends  $82''$  ( $680r_a$ ) and delivers  $8.6 \times 10^{-3} \text{cm}^{-2} \text{s}^{-1}$  of  $H\alpha$ . The low surface brightness of this structure makes an accurate flux measurement difficult.

The left sector of Table 1 contains measured quantities. Our goal here is to compare these observations with the estimates of §2. The right sector of the table contains a few inferred quantities, starting with the perpendicular space velocity for the estimated distance. When the distance estimate is from parallax (P), this is reasonably secure. The next column gives  $n_{fit} = n_H / \sin^2 i$ , as inferred from equation (4); when we lack a proper motion we assume  $v_{\perp} = 100 \text{km s}^{-1}$ .  $r_{apex}$  gives the ratio of observed apex flux to the maximum for a fully neutral medium given by Equation (10) or Equation (14);

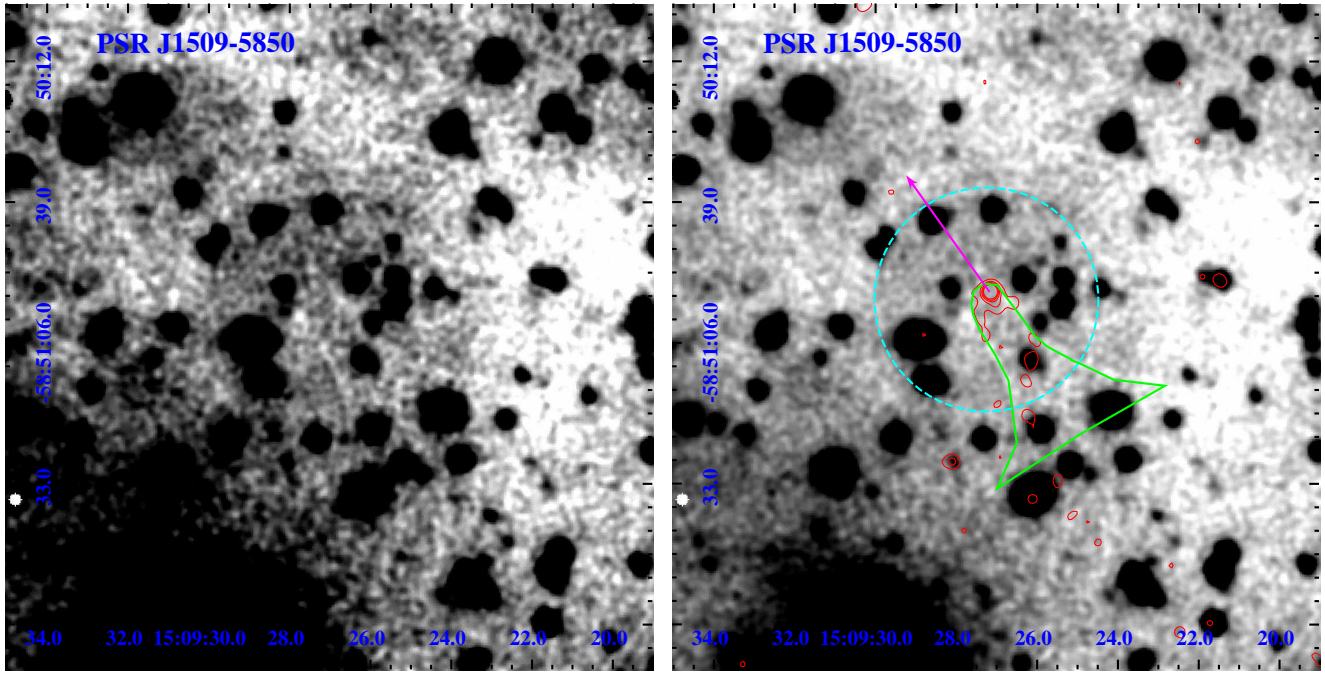


FIG. 5.— Left: a  $2 \times 600$  W012 GHTS image of PSR J1509–5850, smoothed with a  $1.2''$  Gaussian. A faint H $\alpha$  halo surrounds the pulsar, with an edge-brightened bow-shock cavity. The stretch is hard, to bring out low surface brightness structure. The right panel indicates the pulsar proper motion inferred from the X-ray trail. A dashed circle shows the halo and a solid outline shows the bow shock cavity. Superimposed are 0.7–7 keV contours from an archival CXO image (see Kargaltsev et al. 2008). The pulsar point source lies slightly off the bow shock axis, but the extended X-rays outline the apex.

TABLE 1  
PULSARS WITH H $\alpha$  BOW SHOCKS

Pulsar	$\dot{E}_{34}^a$ erg/s	Lg $\tau$ y	$d^b$ kpc	$\mu_T$ mas/y	$F_\gamma^c$ $10^{-11}$	$F_{x,NT}^c$ $10^{-13}$	$\theta_a$ "	$F_{\alpha H\alpha}$ $\gamma/\text{cm}^2/\text{s}$	$r/r_a$	$F_{TH\alpha}$ $\gamma/\text{cm}^2/\text{s}$	$A_R$ mag	$v_\perp$ km/s	$n_{fit}$ $\text{cm}^{-3}$	$r_{apex}$ max	$\theta_I$ "
J0437–4715	0.55	9.8	0.16 P	141.3	1.67	7.9	9.3	6.7E-3	5	1.1E-2	0.01	107	0.21	0.87	1.2
J0742–2822	19.0	5.2	2.0 D	29.0	1.72	<0.2	1.4	1.8E-4	>70	7.6E-3	0.87	275	0.28	1.09	<0.2
J1509–5850	68.2	5.2	2.6 D		12.70	3.0	1.2	1.4E-4	30	6.6E-3	3.51	–	6.14	0.98	8.2
J1741–2054	12.6	5.6	0.38 D		11.70	2.0	2.3	4.6E-3	6	7.6E-3	0.66	–	1.44	2.68	0.9
J1856–3754	3.E-4	6.5	0.16 P	332.0	–	0.0	0.85	3.E-5	>25	9.0E-5	0.06	252	.003	29.6	0.4
											A1	252	0.05	1.25	0.4
J1959+2048	21.9	9.5	2.5 D	30.4	1.7	0.7	3.6	1.8E-3	17	5.6E-3	0.17	360	0.02	11.4	0.5
J2030+4415	2.90	5.8	0.9 G		5.8	2.8	1.1	1.8E-3	10	9.3E-3	0.50	–	2.69	2.05	2.4
J2124–3358	0.68	9.8	0.30 P	52.7	3.7	0.8	5.0	5.3E-4	25	5.6E-3	0.12	75	0.47	0.14	0.3
J2225+6535	0.16	6.1	1.86 D	182.0	–	0.0	0.12	3.6E-5	100	4.6E-3	0.57	1610	0.01	240.	0.0
			1.00								A2	866	1.43	1.42	0.0

Tabulated quantities, in order: Pulsar name, spindown power, characteristic age, distance/method, transverse proper motion, GeV flux, PSR/PWN head X-ray non-thermal flux, estimated standoff angular scale, apex H $\alpha$  flux, full nebula to apex size ratio, full nebula H $\alpha$  flux, estimated extinction, perpendicular velocity, fit total upstream density, ratio of observed apex flux to model flux, characteristic ionization angular scale. See text for details.

<sup>a</sup> Computed at the nominal distance  $d$ . All young pulsars are assumed to have  $M = 1.4 M_\odot / I_{45} = 1.3$ . For PSR J0437–4715 Verbiest et al. (2008) measure  $M = 1.76 \pm 0.2$ , for J1959+2048 van Kerkwijk & Kulkarni (2011) measure  $M = 2.40 \pm 0.12$ ; other MSP are assigned  $M = 1.8 M_\odot / I_{45} = 1.9$ . The spindown power for PSR J1856–3754 comes from X-ray timing (van Kerkwijk & Kaplan 2008).

<sup>b</sup> Distance from D=dispersion measure, G= $\gamma$ -ray flux, P=parallax.

<sup>c</sup> X-ray and  $\gamma$ -ray fluxes in  $\text{erg cm}^{-2}\text{s}^{-1}$ . Values are from 2PC, except for J1741, J2030 (X-ray re-measured) and J1856, J2225 (undetected in  $\gamma$ -ray).

again  $v_\perp = 100 \text{ km s}^{-1}$  is assumed if we have no information.

Most apex values agree well with the model, especially considering the measurement difficulties and approximations involved in generating our model scaling laws. Three pulsars stand out as glaring exceptions. For PSRs J1856–3754 (in the total ionization limit), J1959+2048 and J2225+6535, the model ISM density  $n_{fit}$  is very small and the flux ratio  $r_{apex}$  very large. In particular the J2225+6535 apex is  $240\times$  brighter than expected. Two factors contribute to this mismatch. The assumption of complete post-shock ionization cannot be true for the low luminosity non-LAT pulsars J1856–3754 and J2225+6535, since in this limit they have  $l/r_a = 345$  and  $280$  (at  $1.86 \text{ kpc}$ ), respectively. Thus the gas

is only partly ionized before it reaches the contact discontinuity; Equation (11) determines whether ambient ionization or post shock ionization dominate. For PSR J1856–3754 we find that the upstream ionization will maintain case A1 if  $x_i > 0.043$ . This would lead to a fit upstream density of  $0.052 \text{ cm}^{-3}$  and a model apex flux of  $2.4 \times 10^{-5} \text{ cm}^{-2}\text{s}^{-1}$  ( $r_{apex}=1.25$ ). Slightly higher preshock ionization (likely, considering this pulsar’s modest, but non-negligible, ionizing X-ray flux; §4.4) increases the allowed density and lowers the apex flux. If the density is too high, with low  $x_i$ , then case A2 applies. Then equations 13 and 14 give a density  $n = 0.10 \text{ cm}^{-3}$  and apex flux  $f_{H\alpha} = 4.6 \times 10^{-5} \text{ cm}^{-2}\text{s}^{-1}$  ( $r_{apex}=0.64$ ). This pulsar is evidently very close to the bor-

der between these two cases, as the predicted fluxes bracket the observed value. For PSR J2225+6535, the critical pre-ionization fraction is 0.1 at  $d = 1.86$  kpc. For higher densities, the model gives  $n = 0.12\text{cm}^{-3}$ , while underpredicting the  $\text{H}\alpha$  flux by  $7.4\times$  (case A1) or  $n = 0.42\text{cm}^{-3}$ , underpredicting  $3.6\times$  (case A2), for lower preionization densities.

The third object in question is J1959+2048, an energetic LAT pulsar. With  $l/r_a = 0.06$  this should reach full ionization in the post-shock flow. However J1959+2048 (and, at present, J2225+6535) have only DM distance estimates. With the strong  $d_{\text{kpc}}^{-2}$  and  $d_{\text{kpc}}^{-7/2}$  dependencies in Equations (4) and (10), even modest distance revisions can greatly increase the expected flux. For J1959+2048, matching  $r_{\text{apex}}$  via equation (10) gives  $d = 1.25$  kpc, but since the Shklovskii correction is substantially reduced, the fit distance is actually  $d = 1.4$  kpc. At this distance the velocity  $v_{\perp} = 202$  km/s and upstream total density  $n_{\text{fit}} = 0.28\text{cm}^{-3}$  are quite plausible. In this calculation we have used the large  $I_{45} = 2.9$  implied by equation (1); smaller moments of inertia require even smaller distances. For comparison, Aldcroft et al. (2002) found a  $\sim 1.2$  kpc distance from bow shock modeling of this pulsar.

For J2225+6535, while incomplete post-shock ionization increases the expected flux, the model at  $d = 1.86$  kpc is still at least  $3.6\times$  fainter than observed. In table 1 we show that the case A2 calculation for 1 kpc gives an expected flux 70% of that seen. In fact the values match at 0.8 kpc. However, for case A2 the flux depends on  $n_{\text{H}}$  and thus the measured standoff and  $\theta_a$ . Given the difficulty of defining the apex region and its flux, even with *HST*, we should only infer  $d \approx 1$  kpc for this pulsar. Similarly the  $n_{\text{fit}} = 1.4\text{cm}^{-3}$  density estimate is very sensitive to the poorly resolved (and apparently variable) standoff angle. A high precision parallax distance will be particularly interesting as it will drive improved understanding of the emission of this peculiar shock.

PSRs J0437–4715, J0742–2822 and J1509–5850 have  $r_{\text{apex}} \approx 1$ . The small value for J2124–3358 implies a relatively low neutral fraction in the upstream medium. A more detailed analysis of the shock apex, including anisotropy of the pulsar wind is needed for a more precise estimate of the neutral fraction. For the last two pulsars very modest  $< 25\%$  adjustments to the DM distances bring them into line. For J1741–2054, the apex flux suggests  $d = 0.29$  kpc, which seems plausible given the very small DM. For J2030+4415, 8ur only distance estimate is the very crude 0.88 kpc from the observed  $\gamma$ -ray flux. The  $\text{H}\alpha$  apex flux implies  $d = 0.72$  kpc. Thus the expected incomplete postshock ionization for low  $\dot{E}$  pulsars together with adjustment to the relatively uncertain DM distances allows us to model the observed  $r_{\text{apex}}$  for all bow shock pulsars, certainly to within the accuracy of our apex measurements. This success, together with the strong  $d$  dependence implies that the apex flux provides a new, sensitive pulsar distance estimator. We discuss this further below.

#### 4.4. Precursor Ionization Halos?

The diffuse  $\text{H}\alpha$  emission centered on the pulsars in our images of J2030+4415 and, especially, J1509–5850 suggest a new PWN component, an ionization precursor. Such emission is not unanticipated: Blaes et al. (1995) proposed that accreting isolated neutron stars could ionize cometary HII regions and van Kerkwijk & Kulkarni (2001) applied these ideas to J1856–3754. In the latter paper a numerical model was run which, while not matching the edge-brightened shock structure of J1856–3754, predicted an  $\text{H}\alpha$  halo centered on

the pulsar with a PWN-evacuated trail (their Figure 4) which bears some similarity to our image of PSR J1509–5850 (Figure 5). This suggests that pre-shock ionization does produced the  $\text{H}\alpha$  halo. We would like to understand its origin and its dominance for J1509–5850, in contrast to other pulsar bow shocks.

J1509–5850 has substantially the largest spin-down luminosity in our bow shock set, suggesting that the non-thermal flux dominates the pre-ionization. A useful quantity is ionization standoff angle

$$\theta_I \approx \int \alpha_{\text{ion}}(\nu) \dot{N}_{\text{ion}}(\nu) d\nu / (\pi v d) \quad (17)$$

where  $\alpha_{\text{ion}} = 2.0 \times 10^{-23} E_{\text{keV}}^{-3} \text{cm}^2$  is the H photo-ionization cross section above 13.6 eV and  $\dot{N}_{\text{ion}}(\nu)$  is the spectrum of the apex region, including the pulsar itself. We will estimate  $\dot{N}_{\text{ion}}$  from X-ray observations of the pulsar/PWN apex. Full surface temperatures of young neutron stars are  $kT \sim 50$  eV while millisecond pulsar thermal emission is often dominated by a smaller, hotter zone. In both cases the ionization is dominated by photons well down on the Rayleigh-Jean portion of the spectrum, so that nearby thermally dominated pulsars (e.g. J1856–3754), may be very bright in the soft X-ray but have modest ionizing flux. In contrast, the power-law magnetospheric flux provides a large photon flux near 13.6 eV. 2PC includes a compilation of 0.3 – 10 keV fluxes for the LAT pulsars so for convenience and uniformity we estimate  $\dot{N}_{\text{ion}}$  from these data. Although more detailed sums can be made for individual well-studied pulsars, this provides convenient assessment of the survey targets. For consistency with 2PC, we assume  $kT \sim 50$  eV for the thermal emission and  $\Gamma = 2$  for the non-thermal power law index. With these assumptions one converts from the unabsorbed 0.3 – 10 keV fluxes, obtaining

$$\int \dot{N}_I(E) \alpha_{\text{ion}}(E) dE = \begin{cases} 1.8 \times 10^{22} F_{X,-13} d_{\text{kpc}}^2 \text{cm}^2 \text{s}^{-1} \\ 4.9 \times 10^{23} F_{X,-13} d_{\text{kpc}}^2 \text{cm}^2 \text{s}^{-1} \end{cases}$$

and

$$\theta_I = \begin{cases} 0.8'' F_{X,-13} / \mu_{\text{masy}} & 50 \text{ eV Thermal} \\ 22'' F_{X,-13} / \mu_{\text{masy}} & \Gamma = 2 \text{ PL} \end{cases} \quad (18)$$

We should exclude the large scale  $\gg \theta_a$  downstream PWN flux from the power law component, but this is not always possible without high resolution (e.g. *CXO*) PWN images. When  $\theta_I > \theta_a$  we may expect pre-ionization and an  $\text{H}\alpha$  halo. PSR J1509–5850 and J2030+4415 have the largest  $\theta_I/\theta_a$  in Table 1.

If  $\theta_I$  is very large, say  $\geq 20''$ , then we would expect an extended halo with low surface brightness and very little neutral hydrogen reaching the termination shock. This would compromise  $\text{H}\alpha$  detection. Evidently, for J1509–5850 this pre-ionization is not complete, since we detect edge brightening around the PWN cavity, indicating excitation and/or charge exchange of remnant neutrals in the compressed ISM. Indeed the large value for  $r_{\text{apex}}$  in Table 1 implies small upstream ionization. However, with a slightly smaller extinction  $A_R$  or smaller pulsar distance, the measurements are consistent with substantial upstream ionization. Clearly better images are needed to obtain accurate bow shock fluxes and remnant HI densities for this novel system.

#### 4.5. $\text{H}\alpha$ Upper Limits



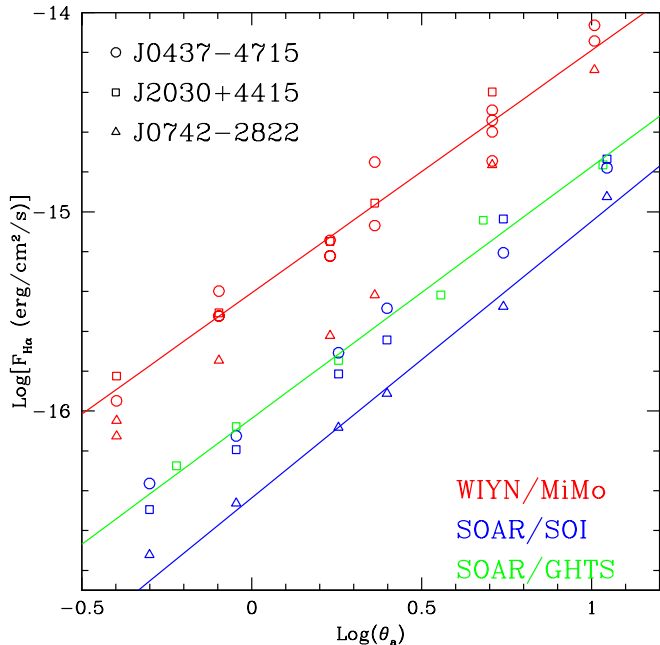


FIG. 6.— Upper limits on undetected bow shocks as a function of standoff scale. Three different bow shocks are used as test templates. The short WIYN/MiMo integrations were read-noise limited. SOAR observations reached larger depth and were limited by background or electronic noise.

We have established that we can detect bow shocks appreciably fainter than those previously reported. However, to extract conclusions from our survey we must both quantify the upper limits for the individual targets and compare these limits with the H $\alpha$  flux expected from these particular sources. This should improve our understanding of the rare bow shock phenomenon, helping future campaigns to discover more examples. With multiple telescope/camera configurations and varying conditions, it is best to quote limits for individual objects. As expected, our limits are essentially surface brightness values. However, for comparison with the sums in §2 we wish to limit the apex flux.

In general, a bow shock nebula stands out *via* its bilaterally symmetric wedge shape. The detectability thus depends somewhat on the nebula geometry. To test this we selected three nebulae, with apex shapes following Equations (5) and (6), scaled these to a range of standoff angular size  $\theta_a$  and apex fluxes  $F_{H\alpha}$ , added them to actual survey images and, via inspection, found the limiting flux below which they would not be noticed. This is perforce somewhat subjective, but clear trends emerged even though the full bow shock shapes varied appreciably from PSR J0437–4715 (apex only), through PSR J2030+4415 (apex plus a single bubble) to PSR J0742–2822 (long low-surface brightness wedge). Figure 6 shows this limiting detection flux as a function of  $\theta_a$ . As expected, when  $\theta_a$  is small, the surface brightness increases and the bow shock can be discerned to fainter  $F_{aH\alpha}$ . The sensitivity depended slightly but not dramatically on the actual shock shape. We can parametrize this limit as

$$F_{aH\alpha} > A\theta_a^{1.3}, \quad \theta_a \gtrsim 0.5'', \quad (19)$$

constant for smaller  $\theta_a$ . Note that this is shallower than the  $\theta_a^2$  for a constant surface brightness limit. The coherent limb of well-resolved nebulae permits detection at lower surface brightness.

The prefactor  $A$  depends on the effective noise in the individual image, particularly on the read-noise, the star field crowding and the presence of diffuse H $\alpha$ . The shorter ex-

posure images (esp. WIYN/MiMo) were read-noise dominated. Longer exposures were limited by crowding or simple S/N. We quantified this by measuring the limiting flux for  $\theta_a = 0.8 - 0.9''$  in each image. For consistency we injected the scaled bow shock of PSR J2030+4415; the test was made at the pulsar position. In most cases this is known to sub-arcsecond precision in our registered images. In addition, when a proper motion was available, we looked for a nebula aligned with this symmetry axis. Tests show that these limits are not strongly dependent on limb shape but are sensitive to the image noise at the pulsar position. In addition the sensitivity for very large  $\theta_a > 10''$  nebulae was found to be slightly decreased when the image had structured diffuse emission.

To convert to an intrinsic flux we need to correct for interstellar extinction. We have used several resources to estimate this value. As an upper limit, we use the full Galactic extinction from Schafly & Finkbeiner (2011), as computed by the NASA Extragalactic Database (NED). For many of our sources, there are extinction estimates listed in 2PC, determined by converting an  $N_H$  estimate from X-ray spectroscopy. In a few cases we supplement these by literature-measured  $N_H$  and follow 2PC in converting to  $A_R = N_H/2.2 \times 10^{21} \text{cm}^{-2}$ . For radio pulsars He, Ng & Kaspi (2013) have computed a  $DM - N_H$  correlation, which gives  $A_R = 0.013DM/\text{cm}^{-3}\text{pc}$ . For the inner Galaxy, we can use the  $A_{K_s}(d)$  compilation of Marshall et al. (2006) to estimate the extinction to our targets at the adopted distance  $d$ . In many cases this provides the only estimate for  $\gamma$ -ray discovered, non-radio PSR. For consistency we adopt the minimum of the various estimates, to provide a lower limit to the foreground extinction, while avoiding bias from intrinsic absorption, etc. The corresponding  $A_R$  values, appropriate for H $\alpha$ , are listed in Table 2.

We did detect stellar continuum sources at the positions of 15 of our binary targets. As it happens, all have previously been reported in the literature, so we do not detail these detections here.

#### 4.6. Detection Statistics and the HI in the ISM

To detect an H $\alpha$  bow shock the pulsar must reside in partly neutral ISM. Thus to compare our measured upper limits with an expected bow shock flux, we must estimate the density and filling fraction of the neutral phases of the ISM. For the cold neutral medium (CNM) we assume high density, resulting in a small volume filling factor. The most important phase for our comparison is the warm neutral medium (WNM) which has a mid-plane density  $\sim 0.3 - 0.6 \text{cm}^{-3}$  and volume filling factor  $\phi \sim 0.35$ . We assume that this is in approximate pressure equilibrium with the warm ionized medium (WIM) and, accordingly, twice the H space density. Kulkarni & Heiles (1987) have used dispersion measure and emission measure observations of the WIM to derive the density and filling factor run with Galactic height  $Z$ . Following their arguments, we can note that WNM and WIM temperatures are very similar so that using their expression for  $\phi_{WIM}(Z)$ , but updating the HI structure to that of Ferrière (2001) we obtain

$$\begin{aligned} \text{CNM} : n_{\text{CNM}} &= 30, & \phi_{\text{CNM}} &= 0.013e^{-(Z/0.13)^2} \\ \text{WNM} : n_{\text{WNM}} &= 0.5 e^{-|Z|/0.43}, & & (20) \\ \phi_{\text{WNM}} &= 0.57 (0.19 e^{-(Z/0.32)^2} + 0.11 e^{-|Z|/0.4})/n_{\text{WNM}} \\ \text{WIM} : n_{\text{WIM}} &= 0.25 e^{-|Z|/0.43}, & \phi_{\text{WIM}} &= 0.1 e^{|Z|/0.75} \end{aligned}$$

TABLE 2  
PULSARS WITH FLUX UPPER LIMITS

Name	$t_{\text{exp}}^a$ s Tel	$f_{\text{obs}-5}^b$	$d/\text{Type}^c$ kpc	$A_R$ mag	$v_{\perp}$ km/s	$\dot{E}_{34}$	$f_{\text{mod}-5}^d$	$\text{rat}^d$	$\theta_{\text{mod}}$ "	$\theta_I$ "	$n_{\text{WNM}}^e$ $\text{cm}^{-3}$	$\phi_{\text{WNM}}^e$	$\text{Flg}^f$
J0023+0923	600 G	4.1	0.69 D	0.19	100	2.87	174.9	0.234	5.32	0.15	0.13	0.16	0.6
J0030+0451	1200 G	2.6	0.32 P	0.04	8.7	0.65	8331.	0.050	45.29	10.07	0.26	0.32	0.0
J0034-0534	1200 G	2.1	0.54 D	0.08	79.5	2.94	453.8	0.081	8.17	0.01	0.15	0.18	1.0
J0101-6422	1200 G	2.4	0.55 D	0.05	40.8	1.75	730.2	0.085	11.18	<3.25	0.18	0.21	0.0
J0102+4839	1200 W	8.1	2.30 D	0.22	100	3.39	17.99	1.076	1.76	<0.41	0.13	0.15	0.0
J0106+4855	600 W	5.9	3.00 D	0.31	100	3.82	10.94	1.255	1.73	<2.64	0.09	0.12	0.0
J0218+4232	300 W	11.8	2.70 D	0.12	64.1	46.29	381.0	0.861	11.65	20.33	0.07	0.12	0.0
J0248+6021	300 W	58.8	2.00 K	3.52	646.0	27.61	0.57	>99	0.47	<2.91	0.47	0.35	0.0
J0307+7443	600 W	11.0	0.60 D	0.08	100	4.07	361.2	0.246	4.48	-	0.36	0.37	0.6
J0340+4130	600 W	6.6	1.80 D	0.22	100	1.23	10.69	0.753	1.05	<0.38	0.22	0.27	0.6
J0357+3205	300 W	9.6	0.60 G	0.35	100	0.77	52.64	0.511	2.00	2.75	0.34	0.37	0.0
J0533+6759	300 W	11.8	2.40 D	0.65	100	1.09	3.59	4.579	1.16	-	0.09	0.12	0.0
J0554+3107	300 W	6.8	2.07 G	1.18	100	7.28	19.80	0.756	1.65	-	0.40	0.37	0.6
J0605+3757	600 W	11.0	0.70 D	0.27	100	1.80	98.40	0.403	2.41	-	0.40	0.37	0.6
J0610-2100	600 W	7.3	3.50 D	0.15	302.6	0.19	0.09	>99	0.17	<1.39	0.04	0.11	0.0
J0613-0200	600 W	6.6	0.90 P	0.11	46.0	2.31	284.1	0.212	4.92	1.96	0.35	0.37	0.0
J0614-3329	600 S	4.2	1.90 D	0.09	100	4.27	37.55	0.503	2.84	2.80	0.09	0.12	0.6
J0622+3749	1200 W	4.8	1.89 G	0.44	100	3.53	22.72	0.487	1.72	<5.09	0.21	0.26	0.6
J0631+1036	300 W	10.3	6.50 O	0.87	100	22.51	8.23	1.203	0.87	<1.53	0.44	0.36	0.0
J0633+0632	300 W	11.0	1.06 G	0.34	100	15.54	350.9	0.239	4.29	3.91	0.48	0.35	0.6
J0729-1448	600 W	6.6	3.50 D	1.20	100	36.69	34.17	0.605	2.16	<1.33	0.41	0.37	0.6
J0734-1559	900 W	5.1	1.40 G	0.88	100	17.21	133.8	0.227	3.53	<3.46	0.44	0.36	0.6
J0737-3039	360 G	16.5	1.10 P	0.63	23.0	1.13	162.3	1.004	5.24	-	0.41	0.37	0.0
J0751+1807	600 W	5.1	0.40 P	0.12	11.4	1.36	6858.	0.085	34.25	2.21	0.35	0.37	0.0
J0908-4913	1200 S	3.8	2.50 D	2.34	100	63.74	40.53	0.610	3.79	<1.03	0.45	0.36	0.6
J1016-5857	1200 S	29.6	2.60 K	1.19	100	334.0	568.4	1.005	8.77	13.56	0.41	0.37	0.0
J1019-5749	600 S	12.7	6.90 D	6.61	100	24.00	0.04	>99	0.88	<10.8	0.41	0.37	0.0
J1023-5746	1200 S	27.5	2.26 G	0.65	100	1417.	5226.	0.279	19.09	4.25	0.48	0.35	0.0
J1024-0719	1800 W	4.4	0.53 D	0.08	150.8	0.09	5.36	0.515	0.63	0.01	0.22	0.27	1.0
J1028-5819	600 S	29.6	2.30 D	0.66	100	108.3	383.6	0.759	5.22	1.08	0.48	0.35	0.6
J1044-5737	1200 S	5.3	1.32 G	0.24	100	104.4	1655.	0.064	9.01	1.27	0.47	0.35	0.6
J1048-5832	600 S	12.7	2.90 D	1.68	100	259.6	226.5	0.730	6.48	3.32	0.47	0.36	0.6
J1105-6107	300 S	38.1	4.90 D	2.20	100	322.1	60.88	5.072	4.50	<0.41	0.42	0.37	0.0
J1119-6127	600 S	14.0	8.40 K	5.11	100	302.9	1.34	40.70	2.56	19.48	0.41	0.37	0.0
J1124-3653	1200 S	3.0	1.70 D	0.22	100	3.08	29.99	0.382	2.55	0.80	0.10	0.13	0.6
J1125-5825	600 S	10.2	2.60 D	0.64	100	15.34	43.34	0.642	1.95	-	0.38	0.37	0.6
J1135-6055	300 S	16.9	3.01 G	0.82	100	268.3	478.6	0.449	6.36	7.05	0.46	0.36	0.0
J1142+0119	1200 W	6.6	0.90 D	0.04	100	0.86	35.14	0.867	2.91	-	0.08	0.12	0.6
J1231-1411	600 W	4.8	0.40 D	0.11	118.2	1.11	168.5	0.171	3.58	1.46	0.25	0.31	1.0
J1301+0833	900 W	2.8	0.70 D	0.06	100	12.65	840.0	0.101	12.60	-	0.10	0.13	0.6
J1311-3430	600 W	3.4	1.40 D	0.14	53.2	9.10	362.3	0.215	10.02	6.60	0.10	0.13	1.0
J1312+0051	1200 W	10.3	0.80 D	0.07	100	1.70	85.66	0.915	4.29	-	0.09	0.12	0.6
J1410-6132	600 S	9.3	15.60 D	8.81	100	1300.	0.06	>99	2.68	<29.3	0.47	0.35	0.0
J1413-6205	600 G	11.4	1.32 G	0.73	100	106.4	1071.	0.211	8.97	1.95	0.48	0.35	0.6
J1418-6058	1800 G	4.0	1.49 G	1.22	100	642.8	3224.	0.066	19.20	0.56	0.50	0.34	0.6
J1420-6048	300 S	5.1	5.60 D	4.66	100	1342.	20.08	4.033	7.57	9.36	0.47	0.35	0.0
J1422-6138	1200 S	5.1	1.64 G	0.86	100	12.54	72.72	0.262	2.49	-	0.48	0.35	0.6
J1429-5911	600 S	6.8	4.08 G	3.52	100	100.7	8.13	4.146	3.09	<3.11	0.40	0.37	0.0
J1446-4701	1800 S	2.5	1.50 D	0.34	100	7.04	78.64	0.144	2.84	<2.35	0.25	0.31	0.6
J1459-6053	600 S	21.2	1.50 G	1.30	100	118.2	548.7	0.732	8.65	1.33	0.45	0.36	0.6
J1514-4946	600 S	5.9	0.90 D	0.41	100	3.03	88.44	0.250	2.48	<0.15	0.39	0.37	0.6
J1522-5734	600 S	7.6	2.29 G	2.34	100	150.5	114.2	0.812	6.15	-	0.48	0.35	0.6
J1531-5610	600 S	6.8	2.10 D	1.44	100	118.6	245.6	0.314	5.85	3.56	0.50	0.34	0.6
J1536-4989	600 G	8.9	1.80 D	0.98	100	2.57	11.07	1.167	1.20	-	0.35	0.37	0.0
J1544+4937	300 W	3.7	1.20 D	0.04	100	2.32	53.63	0.521	4.29	-	0.06	0.11	0.6
J1551-0658	900 W	2.4	1.00 D	0.28	100	0.21	5.60	0.502	1.02	-	0.13	0.15	0.6
J1600-3053	1200 G	2.7	2.40 D	0.43	82.1	1.35	7.34	0.712	1.49	0.02	0.10	0.13	1.0
J1620-4927	600 S	29.6	0.74 G	0.58	100	10.60	388.0	0.705	4.97	<0.52	0.49	0.34	0.6
J1630+3734	1200 W	3.4	0.90 D	0.02	100	2.24	93.37	0.245	3.90	-	0.12	0.14	0.6
J1648-4611	600 S	5.1	4.90 D	4.41	100	27.15	0.67	12.22	1.30	<1.11	0.43	0.37	0.0
J1658-5324	900 S	8.5	0.90 D	0.40	100	5.68	166.9	0.283	3.38	1.17	0.39	0.37	0.6
J1713+0747	900 W	5.9	1.10 P	0.21	32.9	0.63	78.81	0.574	4.33	<6.29	0.16	0.20	0.0
J1718-3825	600 S	25.4	3.60 D	1.78	100	162.5	83.76	2.192	4.12	9.44	0.47	0.35	0.0
J1730-3350	600 G	7.9	3.50 D	3.37	100	160.4	20.28	2.804	4.10	<0.21	0.49	0.34	0.0
J1741+1351	600 W	3.9	0.90 P	0.22	50.1	4.14	405.6	0.151	7.55	<4.32	0.23	0.28	1.0
J1745+1017	300 W	11.0	1.30 D	0.31	48.2	0.81	37.10	1.238	2.70	-	0.18	0.22	0.0

TABLE 2  
PULSARS WITH FLUX UPPER LIMITS (CONTINUED)

Name	$t_{\text{exp}}^a$ s Tel	$f_{\text{obs}-5}^b$	$d/\text{Type}^c$ kpc	$A_R$ mag	$v_{\perp}$ km/s	$\dot{E}_{34}$	$f_{\text{mod}-5}^d$	$\text{rat}^d$	$\theta_{\text{mod}}$ ''	$\theta_I$ ''	$n_{\text{WNM}}$ $\text{cm}^{-3}$	$\phi_{\text{WNM}}$	Flg <sup>e</sup>
J1809–2332	600 W	12.5	1.70 K	1.57	218.0	55.88	48.69	0.937	2.44	12.73	0.43	0.37	0.0
J1810+1744	600 W	9.2	2.00 D	0.14	100	7.59	57.42	0.795	3.09	0.38	0.13	0.15	0.6
J1813–1246	300 G	3.7	1.73 G	0.35	100	811.8	6752.	0.031	20.26	2.48	0.42	0.37	0.6
J1826–1256	300 W	22.0	1.22 G	0.61	100	465.5	6103.	0.204	20.06	3.36	0.49	0.35	0.6
J1833–1034	300 W	8.1	4.30 K	2.20	100	4376.	1071.	0.391	18.76	>99.9	0.43	0.37	0.0
J1835–1106	300 W	23.5	2.80 D	1.72	824.6	23.13	0.88	>99	0.26	<0.10	0.42	0.37	0.0
J1838–0536	600 W	7.0	1.98 G	1.40	100	771.7	1863.	0.157	15.93	1.83	0.49	0.35	0.0
J1846+0919	300 W	14.0	1.53 G	0.88	100	4.44	29.15	1.215	1.84	<4.66	0.36	0.37	0.0
J1902–5105	1200 G	2.4	1.20 D	0.13	100	12.82	271.9	0.098	5.79	<0.71	0.17	0.20	0.6
J1907+0602	600 G	2.3	1.42 G	1.07	100	367.3	2360.	0.039	15.65	0.85	0.47	0.35	0.6
J1954+2836	600 W	5.5	1.74 G	0.66	100	136.4	848.5	0.106	7.68	<1.37	0.49	0.35	0.6
J1957+5033	300 W	10.3	0.91 G	0.25	100	0.67	21.80	0.715	1.24	<0.31	0.33	0.37	0.6
J2017+0603	300 W	9.6	1.60 D	0.31	100	2.55	25.81	0.980	1.90	0.18	0.17	0.21	0.0
J2021+4026	600 W	29.4	1.50 K	1.57	100	14.89	53.65	2.727	3.09	0.28	0.44	0.36	0.0
J2028+3332	600 W	8.8	0.99 G	0.44	100	4.52	106.5	0.326	2.58	<1.62	0.44	0.36	0.6
J2043+1711	600 W	14.7	1.80 D	0.16	111.1	2.19	17.16	1.618	1.47	<1.66	0.16	0.19	0.0
J2051–0827	600 G	3.0	1.00 D	0.19	34.7	1.00	140.9	0.244	5.92	0.01	0.15	0.18	0.0
J2111+4606	300 W	13.2	4.90 D	1.32	100	186.8	79.41	1.025	3.64	<11.5	0.37	0.37	0.0
J2129–0429	1200 G	3.5	0.90 D	0.09	100	4.04	157.8	0.191	4.76	–	0.14	0.16	0.6
J2139+4716	300 W	14.7	0.86 G	0.44	100	0.41	12.71	1.157	0.90	<2.87	0.43	0.37	0.0
J2214+3002	300 W	10.3	1.54 D	0.16	100	3.71	46.64	0.952	2.77	1.20	0.13	0.15	0.0
J2215+5135	300 W	14.7	3.01 D	0.18	100	9.87	31.78	0.918	1.52	2.42	0.30	0.35	0.0
J2234+0944	300 W	13.2	0.80 D	0.24	100	3.08	133.2	0.824	4.58	–	0.15	0.17	0.6
J2238+5903	300 W	16.9	2.11 G	3.08	100	115.6	52.25	3.691	5.86	<9.91	0.48	0.35	0.0
J2240+5832	300 W	19.1	7.70 O	3.08	801.0	28.55	0.04	>99	0.10	<4.62	0.48	0.35	0.0
J2241–5236	1200 G	2.4	0.50 D	0.03	100	6.22	831.0	0.058	9.14	0.27	0.19	0.23	0.6
J2256–1024	300 W	12.5	0.60 D	0.09	100	9.83	862.9	0.366	10.80	–	0.15	0.18	0.6
J2302+4442	300 W	8.8	1.20 D	0.18	100	0.71	14.47	0.810	1.12	0.85	0.25	0.31	0.6
J2339–0533	2400 G	2.5	0.40 D	0.07	100	4.21	850.3	0.056	8.81	0.96	0.21	0.27	0.6

Tabulated quantities, in order: Pulsar name, W012 exposure and camera, measured H $\alpha$  flux limit at fixed scale, distance and method, estimated extinction, adopted perpendicular velocity, spindown power, expected flux for the WNM model, ratio of observed limit to model flux at the model angular scales, model angular scale, ionization angular scale, model local WNM density, model local WNM fill factor, detectability flag. See text for details.

<sup>a</sup> Letter denotes Telescope/camera: G=SOAR/GHTS, S=SOAR/SOI, W=WIYN/MiMo

<sup>b</sup> H $\alpha$  flux upper limit for J2030+4415 template at  $\theta_a = 0.9''$  scale in units of  $10^{-5} \text{cm}^{-2} \text{s}^{-1}$ .

<sup>c</sup> Distance Type codes are from 2PC; D=DM, G= $\gamma$ -ray (Equation 16), K=kinematic, O=other, P=parallax

<sup>d</sup> Model flux in  $10^{-5} \text{cm}^{-2} \text{s}^{-1}$ ;  $\text{rat} = f_{\text{obs}-5} / f_{\text{mod}-5}$ .

<sup>e</sup>  $n_{\text{WNM}}$  and  $\phi_{\text{WNM}}$  are the model WNM density and fill factor at the pulsar  $Z$ .

<sup>f</sup> Flg=0 when known parameters imply no H $\alpha$  bow shock; 1.0 when  $v_{\perp} > 100 \text{km/s}$ , 0.6 otherwise.

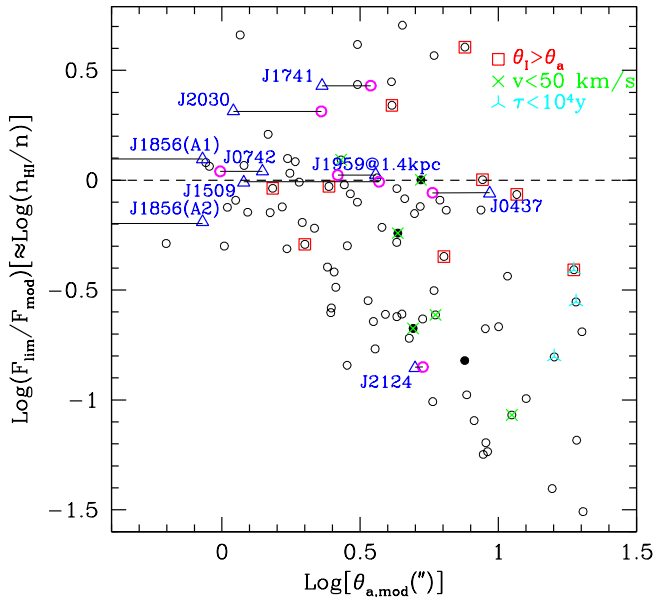


FIG. 7.—  $H\alpha$  survey flux upper limits (as a fraction of the apex model flux, assuming residence in the WNM) plotted against the model apex scale  $\theta_a$ . Points lying below the dashed line give meaningful upper limits on the local neutral fraction; low values suggest the pulsar lies in an ionized medium (eg. WIM). Solid points have parallax distances. Overlays on survey points indicate various conditions counter-indicating a bright bow shock (squares: likely upstream photoionization, x: velocity likely too low for a strong shock, 3-point star: a young pulsar likely close to ionizing SNR or parent association). For comparison, triangles show the detected bow shocks at the observed  $\theta_a$ , lines connect to the model  $\theta_a$  estimates at typical WNM density; the vertical position indicates the apex flux relative to the model at the Table 1  $d$ . Note that most observations give significant sensitivity at the modeled flux. However PSRs J0742–2822 and J2124–3358 lie relatively close to the survey sensitivity boundary; scaled with distance, we would expect to detect nebulae like these  $\sim 30\%$  of the time. We have little sensitivity to pulsars like J1856–3754 (plotted for both Case A1 and Case A2). Given the WNM filling factor and other constraints, we expected to detect  $\sim 9$  sources. Seven LAT pulsars are detected; our survey has contributed three.

with scales in kpc and number densities in  $\text{cm}^{-3}$ . We assume ionization fractions of 0.0, 0.05 and 0.95 for these three phases (Sembach et al. 2000). Kulkarni & Heiles (1987) discuss the possibility that the WIM is over-pressured with respect to the WNM, which would then halve the WNM density and double its fill factor.

We now apply the modeling of §2 to our survey observations. For each pulsar we use the distance and plane height  $Z = d \sin(b)$  to compute the local WNM density and filling factor (Eqs. 20), the resulting apex standoff angle  $\theta_a$  (Eq. 4) and the expected apex flux  $f_{H\alpha}$  (Eq. 10), using measured pulsar parameters whenever possible. The model  $H\alpha$  flux is subject to our estimated extinction §4.5. This number is then compared with our measured upper limit, scaled (Equation 19) for our estimated  $\theta_a$ . We tabulate the resulting ratio in Table 2. When this ratio is  $< 1$ , we have adequate sensitivity to detect the predicted bow shock flux.

We can also use the cataloged X-ray fluxes (from 2PC) to estimate the ionization angle (Eq. 18). We compute for both thermal and non-thermal fluxes; the non-thermal emission nearly always dominates and the combined  $\theta_I$  is listed in Table 2. Even when we have enough sensitivity to detect a bow shock, an  $H\alpha$  nebula may not exist. In particular, we require a strong shock. Here we take  $v_{\perp} > 50 \text{ km/s}$ , recognizing that some pulsars may have  $\sin i \ll 1$  and shock with small transverse velocity. Of the  $\sim 100$  objects covered in this survey only 20 had measured proper motions. Although pul-

sars are a high velocity population with  $v_{2D} \approx 300 \text{ km s}^{-1}$ , we were surprised to find that 8 of 20 had  $v_{\perp} < 50 \text{ km/s}$ . Thus we conservatively assume that as many as 40% of the pulsars without parallax measurements may be too slow to produce robust  $H\alpha$  bow shocks. In addition, very young pulsars lie within their parent supernova remnants and have not escaped to the external neutral medium. We assume that pulsars with  $\log \tau < 4$  are unlikely to show bow shocks. Finally if  $\theta_I > \theta_a$  the ISM may be sufficiently pre-ionized to render a bow shock undetectable. Combining these factors, if a pulsar has  $\log \tau > 4$ ,  $\theta_a > \theta_I$  and  $r < 1$ ,  $P_{det} = \phi_{WNM}$  if a measured proper motion gives  $v_{\perp} > 50 \text{ km/s}$ ,  $P_{det} = 0.6 \phi_{WNM}$  if  $\mu_T$  is unmeasured.  $P_{det} = 0$  otherwise. For our survey  $\Sigma P_{det} = 9.1$  for the WNM. We expect less than one detected bow shock in the CNM and WIM. The total number of observed LAT pulsars that satisfy our survey criteria is seven.

While we only report three new detections, the other four objects would certainly have been (prime) targets in our survey, and easily discovered. The 31% Poisson probability of seven or fewer detections is not unacceptably small. Systematic effects could bias our predicted model flux or our survey sensitivity somewhat high. The total numbers are not very sensitive to our mass-moment of inertia assumptions; assuming that all pulsars have  $M = 1.4 M_{\odot}$  reduces  $\Sigma P_{det}$  to 8.6. If we under-estimated the extinction or overestimated our sensitivity by  $4\times$  we would bring the number of expected detections to  $\sim 3$ . Similarly, increasing all non-parallax distance estimates by  $2\times$  would bring the detections under 4. Alternatively we could assume that pulsars with  $\text{Log}(\tau) < 5.2$  (the youngest bow shock seen) are still in high mass star forming regions with little HI; this brings the expected number down to 5.5. However such radical changes seem unlikely, especially since the model predicts the observed fluxes well and under-predictions fluxes for bow shocks with DM over-estimates.

One interpretation is that our survey argues against a very large filling fraction for the WNM. Our present model implies  $\phi_{WNM} = 0.37$  at mid-plane, but other pictures suggest an even larger filling factor. As noted, if the WNM is under-pressured by  $2\times$  this doubles its filling fraction. The expected bow shock number also doubles, giving a Poisson probability of seven or fewer detections of 0.25%, which seems unacceptable. A larger  $H\alpha$  bow shock sample would help refine these conclusions. With very high sensitivity, we should also discover bow shocks in the WIM. As Figure 7 shows, at present we only have a few pulsars observed with sufficient sensitivity for detection in a 95% ionized WIM. It will be interesting if deeper surveys, e.g. with 10m-class telescopes, can recover more of this faint population. The sums above provide guidance to the most favorable targets.

## 5. PRINCIPAL RESULTS AND CONCLUSIONS

In a quest to further understand the rare pulsar  $H\alpha$  bow shocks we have observed a large sample of energetic, *Fermi* LAT-detected pulsars; sensitive re-measurement of known examples provided context for survey imaging of nearly 100 new targets. Three new  $H\alpha$  shocks were discovered, including the detection of two examples of previously unobserved ionization precursors (PSRs J1509–5850 and J2030+4415).

To interpret these data we have developed a simple analytic model that describes well the apex zone of all known pulsar bow shocks, including conditions likely to produce precursor halos. This analysis provides a good understanding of the apex zone’s angular scale and flux, treating both the high powered pulsars selected by the LAT and the low

$\dot{E}$  nearby pulsars such as PSR J1856–3754 and J2225+6535 which apparently feature incomplete ionization in the post-shock flow. This exercise provides a quantitative connection between the bow shock flux and pulsar parameters, applicable over a range of, e.g.  $10^6\times$  in spindown luminosity. We argue (equation 10) that the flux is independent of ISM density and highly sensitive to the pulsar distance. When the distance is poorly known, bow shock observations provide independent measurements of this crucial parameter. We derive a 0.72 kpc distance for the  $\gamma$ -ray only pulsar J2030+4415. We show that the dispersion measure distances for the millisecond pulsar J1959+2048 and the young, fast PSR J2225+6535 are too large, deriving  $d \approx 1.4$  kpc and  $d = 0.8 - 1$  kpc for these two objects. These distance estimates do depend weakly on velocity inclination  $i$ , the upstream neutral fraction  $f_{HI}$  and, possibly, pulsar wind anisotropy, but these factors can be constrained by measurements of the bowshocks' apex shape and emission line profile. Foreground extinction also affects the estimate, but this can be determined by measuring the nebula Balmer decrement or other absorption studies. Thus pulsar bow shocks, while rare, can provide important new insight into pulsar distances and energetics.

One aspect of this study deserves special attention. The bow show apex covers a large solid angle as viewed from the pulsar and thus provides comprehensive measurement of its mechanical spin-down energy deposition. When a pulsar has a well-measured distance and proper motion, then the bow shock flux puts a lower limit on  $\dot{E}$ , which implies a lower limit on the neutron star moment of inertia. PSR J0437–4715 is the premier example. Our apex flux of  $(6.7 \pm 0.7) \times 10^{-3} \text{H}\alpha \text{ cm}^{-2} \text{s}^{-1}$  translates to a lower limit of  $I_{45} > 1.5$  if the pulsar motion is in the plane of the sky and upstream medium is 100% neutral. Since  $\sin i$  and  $f_{HI}$  are  $\leq 1$ , accounting for these factors will only increase this lower bound. There is in addition a small increase since the photon ( $\gamma$ -ray) energy losses do not contribute to the mechanical losses in the wind, but for PSR J0437–4715 this accounts for  $\sim 1\%$  of  $\dot{E}$  (lower luminosity MSP can be substantially more  $\gamma$ -efficient). The extinction is small and adds little uncertainty to the luminosity of this well-observed bow shock. We have assumed a spherical pulsar wind, but this can be tested by detailed modeling and measurement of the apex H $\alpha$  velocity structure. There is one significant assumption in our computation, that the  $e^-$  and ions equilibrate (Equation 9); if we use the often-assumed  $\epsilon_{\text{H}\alpha} = 0.2$ , our lower bound on the moment of inertia would increase to a (likely unphysical)  $I_{45} > 3.9$ . If the electrons are completely out of equilibrium the implied moment of inertia is even larger.

Since PSR J0437–4715 also has a mass measurement, it should help fulfill the promise of Lattimer & Schutz (2005) that moment of inertia measurements can pin down the neutron star equation of state. Already our estimated  $I_{45} = 1.7 \pm 0.2$  prefers relatively stiff EOS. Other pulsar bow shocks, with their near-bolometric measure of the spin-down power can contribute to this quest. It would be very important to obtain a precise independent parallax of PSR J1959+2058, since the high pulsar mass  $M_{NS} = 2.4M_{\odot}$  implies a very high moment of inertia  $I_{45} = 2.97$ , according to Equation (1). If  $I_{45}$  is lower, one would require an even smaller distance than the  $d = 1.4$  kpc determined in this paper. Of course, one or more young neutron stars with low masses and moments of inertia could also be valuable anchors to the equation of state study. Thus precision parallax measurements of the neutron stars showing H $\alpha$  bow shocks are strongly motivated ingredients in this fundamental physics quest.

Our new images also reveal more details about the post-apex, large scale H $\alpha$  emission. It is now clear that the nebula limb very generally describes a series of undulations or cavities  $10 - 100\theta_a$  downstream. While in some cases, these appear nearly closed, other shocks e.g. PSR J0742–2822 display oscillation about a more or less conical structure. Thus the guitar nebula is only the most spectacular example of down-stream bubbles. The details doubtless depend on accidents of the ISM, but it seems likely that this behavior is a symptom of instabilities in the post-shock PWN flow (van Kerkwijk & Ingle 2008). Surprisingly, we find that with the exception of J1856–3754, the total flux of the observed bow shock nebula are very similar, despite their being detected over a wide range of  $\dot{E}$ ,  $v$  and  $d$ . This calls into question previous efforts to understand the total nebula flux, and suggests that, unlike the apex flux, this does not simply track the pulsar properties.

Finally, our modeling has allowed us to compare our survey flux limits with the expected sizes and fluxes of potential bow shocks around other pulsars. This study implies that the WNM hosting such bow shocks should occupy no more than  $\sim 30\%$  of the nearby Galactic plane. It appears that additional bow shocks await detection, but that deeper exposures are needed. Our analysis points to a set of high  $\dot{E}$ , low extinction objects as the favored targets for future searches, and suggests that intensive study of these nebulae can provide new insights into pulsar physics.

We thank Matt Stadnik for assistance with the image reductions and the referee for a careful reading. This work was supported in part by NASA grants NIX08AW30G and NIX10AD11G and NNX12AO68G, along with Chandra Grant GO0-11097X.

## REFERENCES

- Abdo, A.A. et al. 2009, *Science*, 325, 840  
 Abdo, A.A. et al. 2013, *ApJS*, 208, 17 [2PC]  
 Aldcroft, T.L., Romani, R.W. & Cordes, J.M. 2002, *ApJ*, 400, 638  
 Bell, J. F. et al. 1995, *ApJ*, 440, L81  
 Blaes, O., Warren, O. & Madau, P. 1995, *ApJ*, 454, 370  
 Bucciantini, N. & Bandiera, R. 2001, *AA*, 375, 1032  
 Bucciantini, N. 2002, *AA*, 387, 1066  
 Chatterjee, S. & Cordes, J.M. 2002, *ApJ*, 575, 407  
 Chevalier, R.A. et al. 1980, *ApJ*, 235, 186  
 Cordes, J.M. & Lazio, T.J.W. 2002, *arXiv/0207156*  
 Cordes, J.M., Romani, R.W. & Lundgren, S.C. 193, *Nature*, 362, 133.  
 Dopita, M.A & Hua, C.T. 1997, *ApJS*, 108, 515  
 Ferrière, K. M. 2001, *ARAA*  
 Gaensler, B. et al. 2002, *ApJ*, 580, L137  
 He, C., Ng, C.-Y. & Kaspi, V.M. 2013, *ApJ*, 768, 64  
 Heng, K. & McCray, R. 2007, *ApJ*, 654, 923  
 Jones, D.H et al. 2002, *AA*, 389, L1  
 Kargaltsev, O. et al. 2008, *ApJ*, 684, 542  
 Kargaltsev, O. & Pavlov, G.G. 2010, *AIPC*, 1248, 25  
 Kulkarni, S. & Heiles, C. 1987, *ASSL*, 134, 87  
 Kulkarni, S. & Hester, J.J. 1988, *Nature*, 335, 801  
 Lattimer, J. M. & Schutz, B. F. 2005, *ApJ*, 629, 979  
 Marshall, D. J. et al. 2006, *AA*, 453, 635  
 Ng, C.-Y. et al. 2010, *ApJ*, 712, 596  
 Özel, F. et al. 2012, *ApJ*, 757, 55  
 Pletsch, H.J. et al. 2012, *ApJ*, 744, 105  
 Pletsch, H.J. et al. 2013, *ApJ*, 779, 11  
 Ray, P.S. et al. 2012, *ArXiv* 1205.3089

- Raymond, J.C. 2001, *SpaceSciRev*, 99, 209  
Raymond, J.C. et al. 2010, *ApJ*, 712, 901  
Romani, R.W. et al 2010, *ApJ*, 724, 908  
Romani, R.W. & Watters, K.P. 2010, *ApJ*, 714, 810  
Sembach, K.R. et al. 2000, *ApJ*, 528, 310  
Shklovskii, I.S. 1970, *Soviet Astr.*, 13, 562  
Schlafly, E. S. & Finkbeiner, D.P. 2011, *ApJ*, 737, 103  
van Kerkwijk, M.H. & Kulkarni, S. 2001, *AA*, 380, 221  
van Kerkwijk, M.H. & Kulkarni, S. 2011, *ApJ*, 728, 95  
van Kerkwijk, M.H. & Kaplan, D.L. 2008, *ApJ*, 673, L163  
van Kerkwijk, M.H. & Ingle, A. 2008, *ApJ*, 683, 159  
Verbiest, J. et al. 2008, *ApJ*, 679, 675  
Vigelius, M. et al. 2007, *MNRAS*, 374, 793  
Wagner, A.Y. et al. 2009, *ApJ*, 690, 1412  
Watters, K.P. et al. 2009, *ApJ*, 695, 1289  
Wright, S.A. et al. 2005, *AA*, 436, 967  
Wilkin, F.P. 1996, *ApJ*, 459, L31  
Wilkin, F.P. 2000, *ApJ*, 532, 400